Editors' Suggestion

Flat Γ Moiré Bands in Twisted Bilayer WSe_2

G. Gatti,[1,*] J. Issing,[1,*] L. Rademaker,[2,1] F. Margot,[1] T. A. de Jong,[3] S. J. van der Molen,[3] J. Teyssier,[1] T. K. Kim,[4] M. D. Watson,[4] C. Cacho,[4] P. Dudin,[5] J. Avila,[5] K. Cordero Edwards,[1] P. Paruch,[1] N. Ubrig,[1,6] I. Gutiérrez-Lezama,[1,6] A. F. Morpurgo,[1,6] A. Tamai,[1] and F. Baumberger[1,7]

[1]*Department of Quantum Matter Physics, University of Geneva, 24 Quai Ernest-Ansermet, 1211 Geneva, Switzerland*
[2]*Department of Theoretical Physics, University of Geneva, 24 Quai Ernest-Ansermet, 1211 Geneva, Switzerland*
[3]*Huygens-Kamerlingh Onnes Laboratory, Leiden Institute of Physics, Leiden University, Leiden, The Netherlands*
[4]*Diamond Light Source, Harwell Campus, Didcot, OX11 0DE, United Kingdom*
[5]*Synchrotron SOLEIL, L'Orme des Merisiers, Saint Aubin-BP 48, 91192 Gif sur Yvette Cedex, France*
[6]*Department of Applied Physics, University of Geneva, 24 Quai Ernest Ansermet, CH-1211 Geneva, Switzerland*
[7]*Swiss Light Source, Paul Scherrer Institut, CH-5232 Villigen PSI, Switzerland*

(Received 25 November 2022; accepted 26 June 2023; published 25 July 2023)

The recent observation of correlated phases in transition metal dichalcogenide moiré systems at integer and fractional filling promises new insight into metal-insulator transitions and the unusual states of matter that can emerge near such transitions. Here, we combine real- and momentum-space mapping techniques to study moiré superlattice effects in 57.4° twisted WSe_2 ($tWSe_2$). Our data reveal a split-off flat band that derives from the monolayer Γ states. Using advanced data analysis, we directly quantify the moiré potential from our data. We further demonstrate that the global valence band maximum in $tWSe_2$ is close in energy to this flat band but derives from the monolayer K states which show weaker superlattice effects. These results constrain theoretical models and open the perspective that Γ-valley flat bands might be involved in the correlated physics of twisted WSe_2.

DOI: 10.1103/PhysRevLett.131.046401

The bonding characteristics of van der Waals materials naturally lead to moiré superlattices at interfaces with a lattice mismatch or small twist angle. Exploiting this tuning knob in graphene, WSe_2 and other transition metal dichalcogenides (TMDs) revealed a wealth of nontrivial many-body phases that are not observed in the parent materials. Examples include Mott- and Mott-Wigner-like insulating states [1–8], exciton insulators [9,10], magnetism [9,11], superconductivity [12,13], and strange metal phases [5,14].

The correlated phases in semiconductor moiré systems are generally attributed to strong correlations in monolayer K states that form flat minibands in the moiré superlattice [4,15]. However, imaging such minibands in momentum space proved challenging and key questions such as the bandwidth, the magnitude of the minigaps and even from which monolayer valley the minibands derive remain largely open.

Ab initio calculations of $tWSe_2$ and other twisted TMDs are thus far limited to isolated bilayers without substrate or encapsulation and do not include doping or displacement fields [16–21]. Moreover, they disagree over the strength of superlattice effects and the nature of the minibands at the top of the valence band. Most natural 2H TMD bilayers have the valence band maximum (VBM) at the Γ point where states derive from the antibonding metal d_{z^2}/chalcogen p_z orbital. However, in 2H WSe_2 (and $MoTe_2$) the large spin-orbit splitting of the metal $d_{xy}/d_{x^2-y^2}$ derived states at K shifts the global VBM to the K point [22,23]. Recent large scale density functional calculations find that twist angles below ≈3° tip this balance and move the VBM of $tWSe_2$ back to Γ [18]. A VBM at Γ was also reported in an ARPES study of twisted double bilayer WSe_2 [24]. Other calculations for different twist angles [17,20,21,25] and a recent experiment at 5.1° twist angle [26], find that the VBM derives from monolayer K states.

The nature of the VBM states is crucial because the effective low-energy models used to study correlation effects in twisted TMDs differ for Γ and K states. For Γ derived states, theoretical studies find an emergent honeycomb symmetry with a moiré miniband structure that resembles artificial graphene [17,18,20,21]. For K-derived states, on the other hand, recent theoretical work found a parabolic moiré VBM at K of the mini-Brillouin zone (BZ) [18] and an electric field induced topological insulator phase [15]. These differences have obvious implications for the interpretation of transport measurements that are currently being performed and that exhibit a plethora of exciting new phenomena.

The strength of superlattice effects is commonly parametrized by an effective moiré potential. However, estimates of the moiré potential in the literature show a considerable spread ranging from a few millielectron volt (meV) up to hundreds of meV [17,19,27,28]. Previous μ-ARPES studies on $tWSe_2$ and other TMD moiré systems found signatures of replica bands but could not resolve flat bands with the moiré periodicity or estimate the effective moiré potential

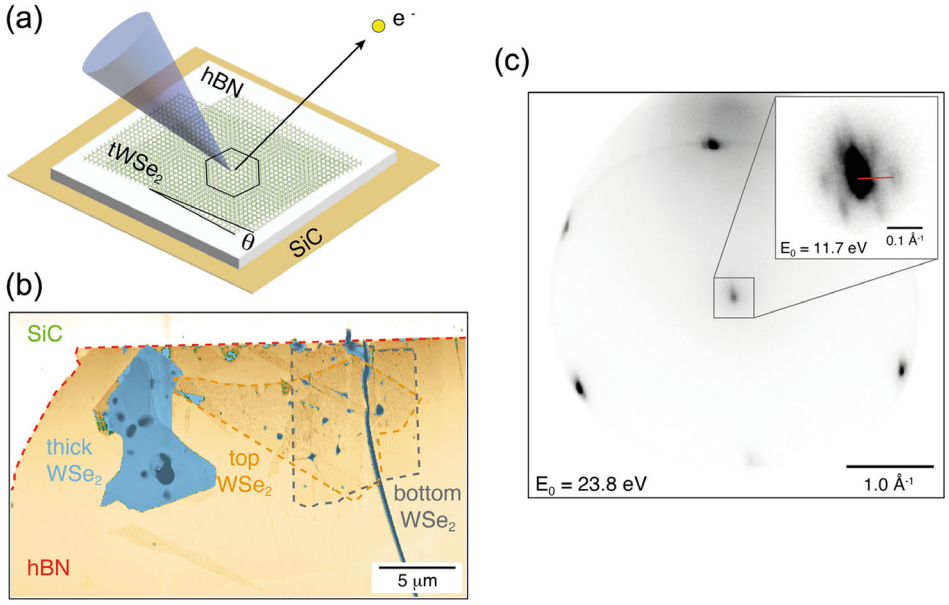

FIG. 1. Device layout and characterization. (a) Schematic of the μ-ARPES experiment on $tWSe_2$. Heterostructures of $tWSe_2$ on hBN were produced with a tear and stack method and studied with synchrotron based microfocus ARPES (for details, see Methods). The black hexagon indicates the moiré unit cell for an arbitrary twist angle θ. (b) Topographic atomic force microscopy image of the van der Waals heterostructure. The scale bar is 5 μm. (c) μ-LEED pattern of the twisted bilayer WSe_2. The inset shows a zoom of the (0,0) spot with the satellite peaks used to quantify the moiré wavelength. The red line indicates a reciprocal moiré superlattice vector.

[26,29,30]. Scanning tunneling microscopy (STM) studies of $tWSe_2$ found that the local density of states is spatially modulated and, depending on energy and twist angle, can have triangular, honeycomb, or Kagome symmetry [26,31,32]. STM further revealed a rich structure of tunneling spectra in the valence band consistent with the formation of moiré minibands. Correlating the real space information from STM with band structure calculations is, however, nontrivial.

Here, we report the direct observation of a flat moiré miniband in $tWSe_2$. The flat band derives from the monolayer Γ states and is in close proximity to the global VBM, opening the possibility that the Γ-valley flat band participates in the correlated phases of $tWSe_2$. We estimate the band width of the moiré miniband and determine the moiré potential from a quantitative analysis of the ARPES data.

Figure 1 illustrates the methodology used in our study. We fabricate the $tWSe_2$ structure with the tear and stack method using a polypropylene carbonate (PPC) stamp, first picking up an hBN flake and then the WSe_2 layers [33]. Prior to the ARPES measurements, we invert the stack, release it on a graphitized SiC substrate and sublimate the PPC in vacuum. This technique avoids any contact of $tWSe_2$ with polymers, which facilitates obtaining a clean, polymer-free sample surface. μ-ARPES experiments were performed at beamline I05 of Diamond Light Source using 90 eV photons [34]. Details of the μ-ARPES experiments and sample fabrication are given in the Supplemental Material [35].

We determine the precise twist angle of the heterostructure used for the μ-ARPES experiments from microfocus low-energy electron diffraction (μLEED) (see Fig. 1). The threefold symmetry of the μLEED patterns in TMDs [44] independently confirms a stacking angle near ≈60°, corresponding to a 2H structure. Note that the threefold symmetry arises from structure factors and does not imply a lifting of the K-K' degeneracy in the electronic structure. An enlargement around the (0,0) specular beam reveals six satellite spots that define a moiré mini-BZ. From fits to μLEED line profiles shown in Supplemental Material [35], Fig. 3, we determine a reciprocal lattice vector $G^{\mathrm{Moir\acute{e}}} \approx 1\ \mathrm{nm}^{-1}$ corresponding to a moiré wavelength of $a_M = 7.3$ nm and a twist angle $\theta = 57.4 \pm 0.1°$. Note that the moiré mini-BZ is rotated by 90° with respect to the atomic BZ defined by the main diffraction spots. Measurements at multiple locations on the $tWSe_2$ indicate a twist angle variation of no more than 0.4° in the sample studied here.

Figure 2 shows the valence band dispersion of $tWSe_2$ over the entire monolayer BZ. At first glance, the overall dispersion is reminiscent of a natural 2H bilayer with parabolic band maxima at Γ and K [22]. However, a closer inspection of the data near Γ [Fig. 2(d)] reveals the presence of additional features on a much smaller energy scale that are absent in untwisted 2H WSe_2. Extracting energy distribution curves (EDC) at Γ from the data in Fig. 2(d), we resolve three distinct components in $tWSe_2$ [features A, B, C in Fig. 2(b)], in stark contrast to the EDC of 2H WSe_2, which shows a single peak only. This splitting into multiple peaks in $tWSe_2$ is a fingerprint of moiré minibands. It also shows that moiré superlattice effects alter valley energies.

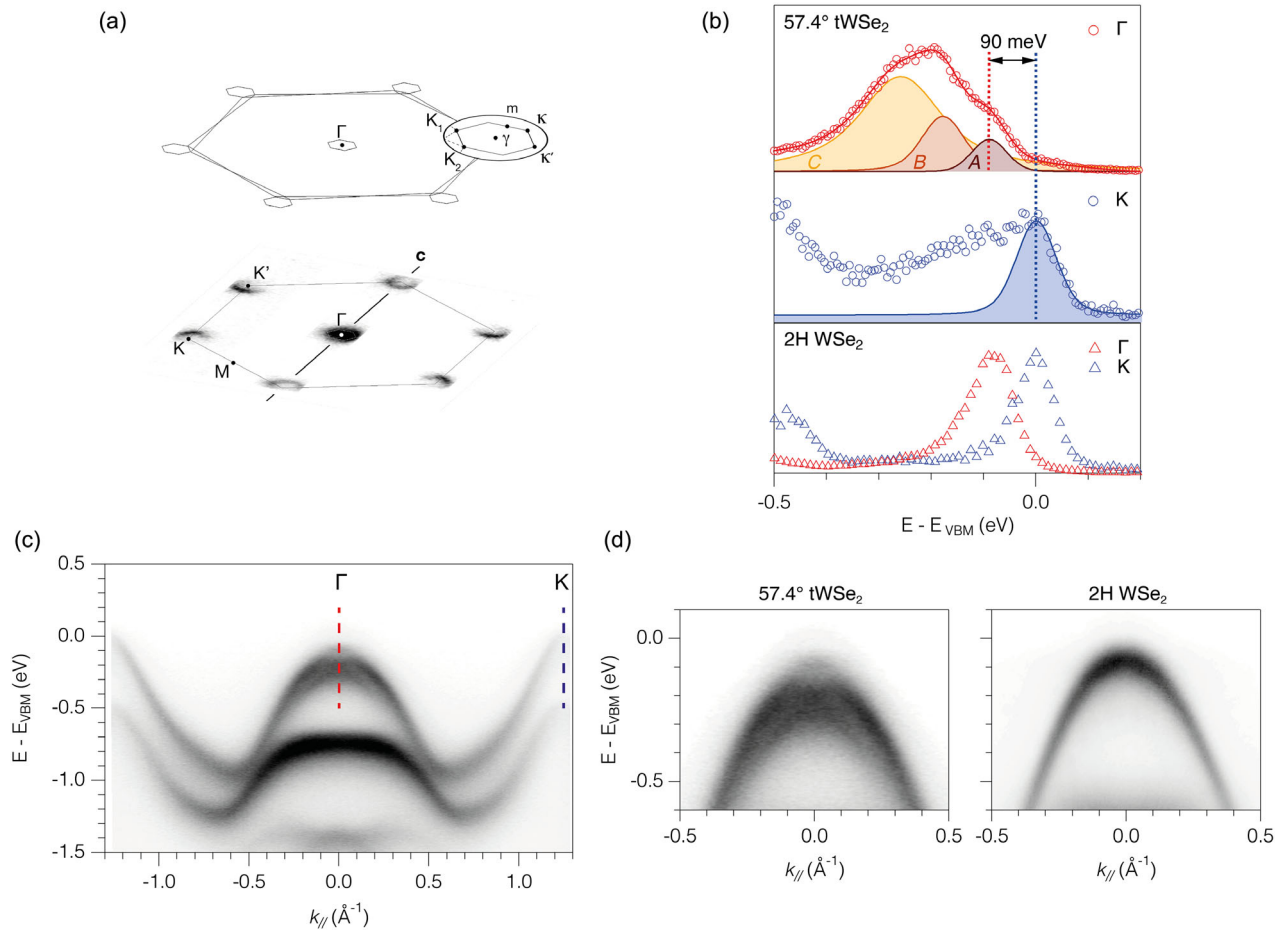

FIG. 2. Valence band maximum in $tWSe_2$. (a) ARPES constant energy map 200 meV below the VBM. The BZs of the two twisted monolayers are indicated by gray hexagons. Small hexagons show the moiré mini-BZs. (b) Energy distribution curves (EDCs) from $tWSe_2$ and untwisted 2H WSe_2 extracted at Γ and K of the monolayer BZ. The EDCs from $tWSe_2$ are fit with three and one Lorentzians, respectively, convolved with a Gaussian of 70 meV full width half maximum to account for energy resolution and inhomogeneous broadening. (c) ARPES band dispersion of $tWSe_2$ measured along ΓK over the large monolayer BZ. (d) Enlargement of the ARPES spectral functions of twisted and untwisted WSe_2 near the Γ point.

None of the 3 components in $tWSe_2$ can be trivially associated with the single peak in 2H WSe_2. This suggests that moiré effects can shift valleys by several ten meV, which is non-negligible in bilayer WSe_2 because of the close proximity in energy of states at Γ and K [22,23,45].

The spectrum at K shows a well-defined onset but no clear multipeak structure. This implies weaker superlattice effects than at Γ, in qualitative agreement with theoretical predictions [17,18]. We quantify valley energies from experiment by comparing the highest-energy feature A in the multipeak fit at Γ with a fit of the onset of spectral weight at K. This shows that the Γ-valley in $tWSe_2$ lies 90 ± 20 meV lower than the global VBM measured at K. This is comparable to the variation of valley energies with strain [46], doping, and displacement fields [47] and only slightly larger than the chemical potential of WSe_2 at relevant densities, all suggesting the Γ-valley flat band might contribute to the correlated phases observed in $tWSe_2$ [4,5,9].

Figure 3(a) shows the complex spectral function of the moiré states along both high symmetry directions. Near the Γ point we can directly trace the dispersion of features A, B, C from curve fits of the EDCs shown in Fig. 3(c). Additional, more dispersive features at higher energy are evident in the raw image and curvature plots of the ARPES data. The topmost feature A defines the first moiré miniband. Consistent with the curvature plots, our fits show that this band is nearly dispersionless and separated by a gap of several 10 meV from other states. Tracing feature A over the full mini-BZ, we estimate a band width of the first moiré miniband of ≈10 meV. This is small compared to the Hubbard interaction estimated as $U \approx e^2/(4\pi\epsilon\epsilon_0 d) \approx 80$ meV (assuming $\epsilon \approx 5$ and $d \approx a_M/2 = 3.6$ nm) placing half-filled 57.4° $tWSe_2$ in the strongly correlated regime.

We now compare our data to a generic effective continuum model describing the motion of electrons in

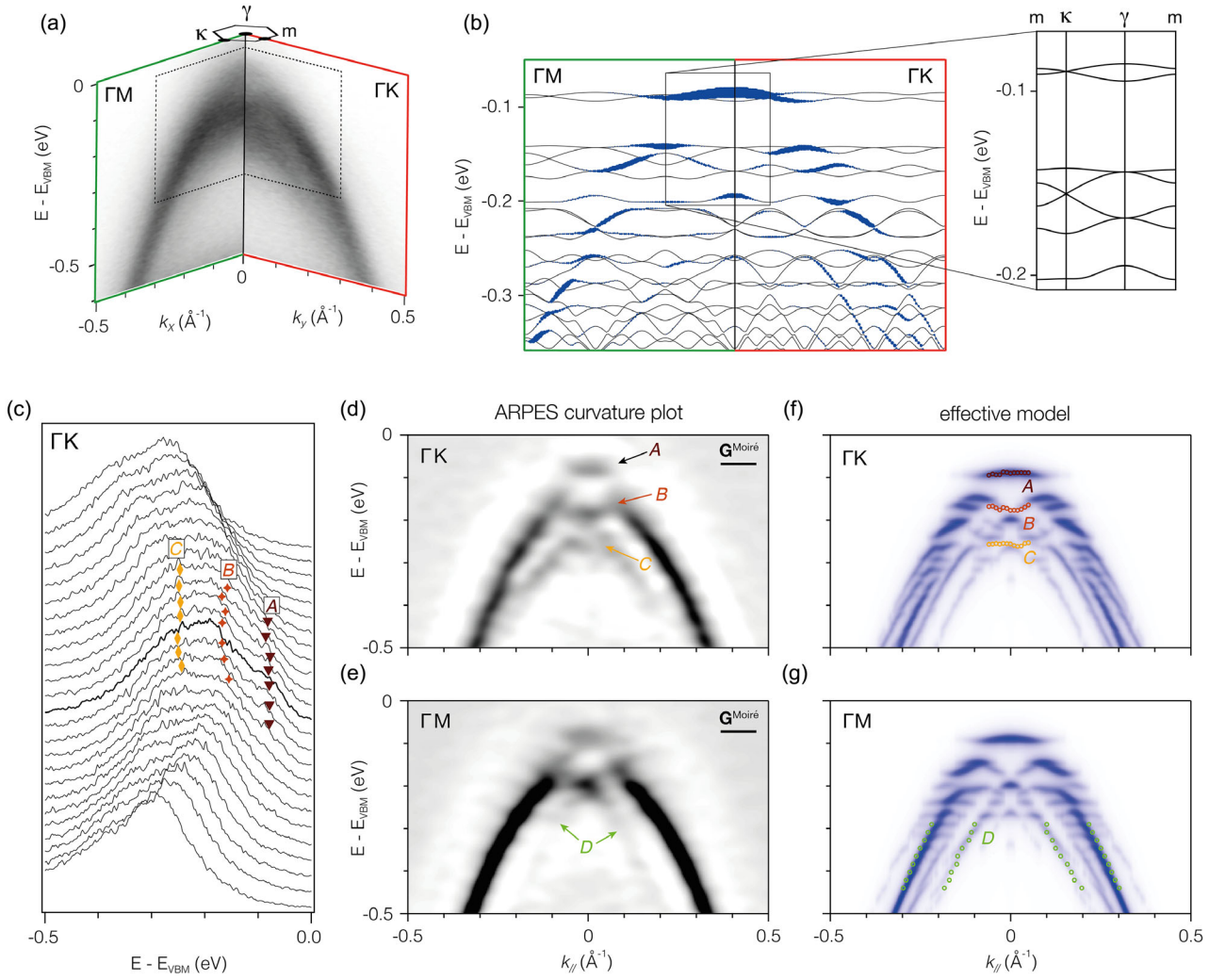

FIG. 3. Moiré minibands. (a) ARPES band dispersions near the Γ point along the two high symmetry directions. The small hexagon indicates the mini BZ. (b) Band dispersion (black) and spectral weights (blue) of the effective Hamiltonian in Eq. (1) with parameters $V_0 = 48$ meV and $\phi = 121°$. (c) Stack of EDCs in a momentum window of 0.2 Å^{-1} along K-Γ-K'. Markers indicate the position of the three Lorentzian peaks obtained from curve fits. (d),(e) Curvature plots of the ARPES band dispersions along the K-Γ-K' and M-Γ-M directions, respectively. The scale bar corresponds to a moiré reciprocal lattice vector. (f),(g) Simulated spectral function of the effective Hamiltonian with the same parameters used in (c). For a visual comparison with the curvature plots in (d),(e) we use a Lorentzian broadening of 10 meV which is smaller than the optimal value found in the numerical optimization (see Supplemental Material, Sec. V [35]).

the bonding and antibonding valence band of twisted TMDs in the presence of an effective moiré potential [19]:

$$H = \begin{bmatrix} -\frac{\hbar^2\mathbf{k}^2}{2m^*} + V_1 & t_\perp(\mathbf{k}) \\ t_\perp(\mathbf{k}) & \frac{\hbar^2\mathbf{k}^2}{2m^*} + V_2 \end{bmatrix}$$

$$V_{1,2} = 2V_0 \sum_{j=1}^{3} \cos(\mathbf{G}_j^{\text{Moiré}} \cdot \mathbf{r} \pm \phi) \qquad (1)$$

Here, the effective mass m^* and interlayer hopping $t_\perp(\mathbf{k})$ parametrize the band structure of untwisted bilayers. We determine both of these parameters from fits to density functional theory calculations. Supplemental Material [35], Fig. 6 shows that this is in excellent agreement with ARPES data from exfoliated 2H WSe_2. The moiré physics is described with the effective potential $V_{1,2}$, which we expand in a first order Fourier series in the moiré wave vectors $\mathbf{G}_j^{\text{Moiré}}$ with phase factors ϕ that change sign with layer to be consistent with the twofold rotational symmetry with layer exchange. This model reproduces the band structure found in previous theoretical work [17,19] with the characteristic Dirac cones at κ in the first moiré miniband for a wide range of phases ϕ [Fig. 3(b)].

For a direct comparison with the ARPES data, we first calculate spectral weights by projecting the eigenstates of

H on plane wave states with momentum $\mathbf{k}$ [48–50]. This strongly suppresses one side of the predicted Dirac cone rendering its direct observation challenging [see Fig. 3(b)]. Performing calculations for different combinations of V_0, ϕ we identify three principal features that are sensitive to the model parameters: (i) As expected from theory, the gap between the first two moiré subbands is controlled by V_0; (ii) the spectral weight distribution of the dispersive features at high binding energy is very sensitive to the phase ϕ, while (iii) the separation of features A, B, C is determined by a combination of V_0 and ϕ. Hence, V_0 and ϕ are sufficiently independent to be determined from our data. To do so in an unbiased way we calculate $> 20'000$ spectral functions for different parameters and determine the least square difference to the raw data. This yields $V_0 = 48 \pm 8$ meV and $\phi = 121° \pm 7°$, where the error bars are estimated from the standard deviation of the parameters of all calculations weighted by the inverse of their square difference to the data. As shown in Supplemental Material, Sec. V [35], these results are robust with regard to realistic variations in the twist angle.

Figures 3(f) and 3(g) show the continuum model spectral functions with the above determined parameters and a reduced broadening, demonstrating a good overall agreement with the data. This confirms the interpretation of the main spectral features in terms of moiré minibands. The calculations clearly reproduce a split-off flat band that is highly localized in momentum space (feature A) suggesting a wave function extending over much of the moiré unit cell. The bandwidth (γ-κ-m dispersion in the mini-BZ) of the first subband in our model is 6 meV, in fair agreement with our experimental estimate of 10 meV.

The calculations also reproduce the weakly dispersive features B, C as well as the sideband D. We note that the latter has been reported previously in Ref. [26] where its separation from the main band was identified with the moiré reciprocal lattice vector. Our calculations show that such an interpretation is not evident as a multitude of dispersive sidebands are expected at various momenta.

The phase $\phi \approx 120°$ determined from our numerical analysis confirms the emergent honeycomb symmetry of the first subband, predicted by large scale density functional theory calculations [17–19]. We note that a honeycomb charge distribution was also reported in some STM spectroscopic imaging experiments [26,31] while another recent STM study found a triangular symmetry for the highest visible subband [32]. Mapping the full twist angle, valley and material dependence of the electronic symmetry in semiconductor moiré superlattices represents a formidable task for future experiments.

Our quantification of superlattice effects in $tWSe_2$ provides a benchmark for large scale DFT calculations. More broadly, our work lends strong support to an interpretation of the remarkable transport and optical properties of $tWSe_2$ in terms of a correlated flat band system. However, our work also shows that $tWSe_2$ lacks the clear separation of energy scales needed for a description by a single band Hubbard model. The moiré potential of $V_0 = 48$ meV determined from our quantitative analysis is comparable to the energy difference of Γ and K valleys and also to shifts in valley energies predicted under realistic doping, displacement field and strain values [46,47]. Moreover, for the twist angle studied here, the on-site interaction U likely exceeds the moiré potential and thus the gap between subband manifolds. Accounting for this complexity will be essential for the interpretation of magnetotransport and optical measurements and will require the development of multiband theoretical models.

The research data supporting this publication can be accessed at the Yareta repository of the University of Geneva [51].

This work was supported by the Swiss National Science Foundation (SNSF) under Grants No. 184998, No. 178891. L. R. acknowledges support from a SNSF Ambizione fellowship 174208 and Starting Grant No. 211296. A. F. M. acknowledges financial support from the SNSF and from the EU Graphene Flagship project. T. A. d. J. acknowledges financial support by the Netherlands Organisation for Scientific Research (NWO/OCW) as part of the Frontiers of Nanoscience (NanoFront) program. We acknowledge Diamond Light Source for time on Beamline I05 under Proposal SI29021.

[*] These authors contributed equally to this work.

[1] E. C. Regan, D. Wang, C. Jin, M. I. Bakti Utama, B. Gao, X. Wei, S. Zhao, W. Zhao, Z. Zhang, K. Yumigeta, M. Blei, J. D. Carlström, K. Watanabe, T. Taniguchi, S. Tongay, M. Crommie, A. Zettl, and F. Wang, Mott and generalized Wigner crystal states in WSe_2/WS_2 moiré superlattices, Nature (London) **579**, 359 (2020).

[2] Y. Tang, L. Li, T. Li, Y. Xu, S. Liu, K. Barmak, K. Watanabe, T. Taniguchi, A. H. MacDonald, J. Shan, and K. F. Mak, Simulation of Hubbard model physics in WSe_2/WS_2 moiré superlattices, Nature (London) **579**, 353 (2020).

[3] Y. Xu, S. Liu, D. A. Rhodes, K. Watanabe, T. Taniguchi, J. Hone, V. Elser, K. F. Mak, and J. Shan, Correlated insulating states at fractional fillings of moiré superlattices, Nature (London) **587**, 214 (2020).

[4] L. Wang, E.-M. Shih, A. Ghiotto, L. Xian, D. A. Rhodes, C. Tan, M. Claassen, D. M. Kennes, Y. Bai, B. Kim, K. Watanabe, T. Taniguchi, X. Zhu, J. Hone, A. Rubio, A. N. Pasupathy, and C. R. Dean, Correlated electronic phases in twisted bilayer transition metal dichalcogenides, Nat. Mater. **19**, 861 (2020).

[5] A. Ghiotto, E.-M. Shih, G. S. S. G. Pereira, D. A. Rhodes, B. Kim, J. Zang, A. J. Millis, K. Watanabe, T. Taniguchi, J. C. Hone, L. Wang, C. R. Dean, and A. N. Pasupathy, Quantum criticality in twisted transition metal dichalcogenides, Nature (London) **597**, 345 (2021).

[6] T. Li, S. Jiang, L. Li, Y. Zhang, K. Kang, J. Zhu, K. Watanabe, T. Taniguchi, D. Chowdhury, L. Fu, J. Shan, and K. F. Mak, Continuous Mott transition in semiconductor moiré superlattices, Nature (London) **597**, 350 (2021).

[7] Y. Shimazaki, I. Schwartz, K. Watanabe, T. Taniguchi, M. Kroner, and A. Imamoğlu, Strongly correlated electrons and hybrid excitons in a moiré heterostructure, Nature (London) **580**, 472 (2020).

[8] H. Li, S. Li, E. C. Regan, D. Wang, W. Zhao, S. Kahn, K. Yumigeta, M. Blei, T. Taniguchi, K. Watanabe, S. Tongay, A. Zettl, M. F. Crommie, and F. Wang, Imaging two-dimensional generalized Wigner crystals, Nature (London) **597**, 650 (2021).

[9] Y. Xu, K. Kang, K. Watanabe, T. Taniguchi, K. F. Mak, and J. Shan, A tunable bilayer Hubbard model in twisted WSe_2, Nat. Nanotechnol. **17**, 934 (2022).

[10] Z. Zhang, E. C. Regan, D. Wang, W. Zhao, S. Wang, M. Sayyad, K. Yumigeta, K. Watanabe, T. Taniguchi, S. Tongay, M. Crommie, A. Zettl, M. P. Zaletel, and F. Wang, Correlated interlayer exciton insulator in heterostructures of monolayer WSe_2 and moiré WS_2/WSe_2, Nat. Phys. **18**, 1214 (2022).

[11] A. L. Sharpe, E. J. Fox, A. W. Barnard, J. Finney, K. Watanabe, T. Taniguchi, M. A. Kastner, and D. Goldhaber-Gordon, Emergent ferromagnetism near three-quarters filling in twisted bilayer graphene, Science **365**, 605 (2019).

[12] Y. Cao, V. Fatemi, S. Fang, K. Watanabe, T. Taniguchi, E. Kaxiras, and P. Jarillo-Herrero, Unconventional superconductivity in magic-angle graphene superlattices, Nature (London) **556**, 43 (2018).

[13] X. Lu, P. Stepanov, W. Yang, M. Xie, M. A. Aamir, I. Das, C. Urgell, K. Watanabe, T. Taniguchi, G. Zhang, A. Bachtold, A. H. MacDonald, and D. K. Efetov, Superconductors, orbital magnets and correlated states in magic-angle bilayer graphene, Nature (London) **574**, 653 (2019).

[14] A. Jaoui, I. Das, G. Di Battista, J. Díez-Mérida, X. Lu, K. Watanabe, T. Taniguchi, H. Ishizuka, L. Levitov, and D. K. Efetov, Quantum critical behaviour in magic-angle twisted bilayer graphene, Nat. Phys. **18**, 633 (2022).

[15] F. Wu, T. Lovorn, E. Tutuc, I. Martin, and A. H. MacDonald, Topological Insulators in Twisted Transition Metal Dichalcogenide Homobilayers, Phys. Rev. Lett. **122**, 086402 (2019).

[16] M. H. Naik and M. Jain, Ultraflatbands and Shear Solitons in Moiré Patterns of Twisted Bilayer Transition Metal Dichalcogenides, Phys. Rev. Lett. **121**, 266401 (2018).

[17] M. Angeli and A. H. MacDonald, Gamma valley transition metal dichalcogenide moire bands, Proc. Natl. Acad. Sci. U.S.A. **118**, e2021826118 (2021).

[18] V. Vitale, K. Atalar, A. A. Mostofi, and J. Lischner, Flat band properties of twisted transition metal dichalcogenide homo- and heterobilayers of MoS_2, $MoSe_2$, WS_2 and WSe_2, 2D Mater. **8**, 045010 (2021).

[19] Y. Zhang, T. Liu, and L. Fu, Electronic structures, charge transfer, and charge order in twisted transition metal dichalcogenide bilayers, Phys. Rev. B **103**, 155142 (2021).

[20] T. Devakul, V. Crépel, Y. Zhang, and L. Fu, Magic in twisted transition metal dichalcogenide bilayers, Nat. Commun. **12**, 6730 (2021).

[21] S. Kundu, M. H. Naik, H. R. Krishnamurthy, and M. Jain, Moiré induced topology and flat bands in twisted bilayer WSe_2: A first-principles study, Phys. Rev. B **105**, L081108 (2022).

[22] N. R. Wilson, P. V. Nguyen, K. Seyler, P. Rivera, A. J. Marsden, Z. P. L. Laker, G. C. Constantinescu, V. Kandyba, A. Barinov, N. D. M. Hine, X. Xu, and D. H. Cobden, Determination of band offsets, hybridization, and exciton binding in 2D semiconductor heterostructures, Sci. Adv. **3**, e1601832 (2017).

[23] J. Lindlau, M. Selig, A. Neumann, L. Colombier, J. Förste, V. Funk, M. Förg, J. Kim, G. Berghäuser, T. Taniguchi, K. Watanabe, F. Wang, E. Malic, and A. Högele, The role of momentum-dark excitons in the elementary optical response of bilayer WSe_2, Nat. Commun. **9**, 2586 (2018).

[24] L. An, X. Cai, D. Pei, M. Huang, Z. Wu, Z. Zhou, J. Lin, Z. Ying, Z. Ye, X. Feng, R. Gao, C. Cacho, M. Watson, Y. Chen, and N. Wang, Interaction effects and superconductivity signatures in twisted double-bilayer WSe_2, Nanoscale Horiz. **5**, 1309 (2020).

[25] S. J. Magorrian, V. V. Enaldiev, V. Zólyomi, F. Ferreira, V. I. Fal'ko, and D. A. Ruiz-Tijerina, Multifaceted moiré superlattice physics in twisted WSe_2 bilayers, Phys. Rev. B **104**, 125440 (2021).

[26] D. Pei *et al.*, Observation of Γ-Valley Moiré Bands and Emergent Hexagonal Lattice in Twisted Transition Metal Dichalcogenides, Phys. Rev. X **12**, 021065 (2022).

[27] S. Shabani, D. Halbertal, W. Wu, M. Chen, S. Liu, J. Hone, W. Yao, D. N. Basov, X. Zhu, and A. N. Pasupathy, Deep moiré potentials in twisted transition metal dichalcogenide bilayers, Nat. Phys. **17**, 720 (2021).

[28] W. T. Geng, V. Wang, Y. C. Liu, T. Ohno, and J. Nara, Moiré potential, lattice corrugation, and band gap spatial variation in a twist-free $MoTe_2/MoS_2$ heterobilayer, J. Phys. Chem. Lett. **11**, 2637 (2020).

[29] C. H. Stansbury *et al.*, Visualizing electron localization of WS_2/WSe_2 moiré superlattices in momentum space, Sci. Adv. **7**, eabf4387 (2021).

[30] S. Xie, B. D. Faeth, Y. Tang, L. Li, E. Gerber, C. T. Parzyck, D. Chowdhury, Y.-H. Zhang, C. Jozwiak, A. Bostwick, E. Rotenberg, E.-A. Kim, J. Shan, K. F. Mak, and K. M. Shen, Strong interlayer interactions in bilayer and trilayer moiré superlattices, Sci. Adv. **8**, eabk1911 (2022).

[31] Z. Zhang, Y. Wang, K. Watanabe, T. Taniguchi, K. Ueno, E. Tutuc, and B. J. LeRoy, Flat bands in twisted bilayer transition metal dichalcogenides, Nat. Phys. **16**, 1093 (2020).

[32] E. Li, J.-X. Hu, X. Feng, Z. Zhou, L. An, K. T. Law, N. Wang, and N. Lin, Lattice reconstruction induced multiple ultra-flat bands in twisted bilayer WSe_2, Nat. Commun. **12**, 5601 (2021).

[33] K. Kim, M. Yankowitz, B. Fallahazad, S. Kang, H. C. P. Movva, S. Huang, S. Larentis, C. M. Corbet, T. Taniguchi, K. Watanabe, S. K. Banerjee, B. J. LeRoy, and E. Tutuc, Van der Waals heterostructures with high accuracy rotational alignment, Nano Lett. **16**, 1989 (2016).

[34] M. Hoesch, T. K. Kim, P. Dudin, H. Wang, S. Scott, P. Harris, S. Patel, M. Matthews, D. Hawkins, S. G. Alcock, T. Richter, J. J. Mudd, M. Basham, L. Pratt, P. Leicester, E. C. Longhi, A. Tamai, and F. Baumberger, A facility for the analysis of the electronic structures of solids and their surfaces by synchrotron radiation photoelectron spectroscopy, Rev. Sci. Instrum. **88**, 013106 (2017).

[35] See Supplemental Material at http://link.aps.org/supplemental/10.1103/PhysRevLett.131.046401 which includes Refs. [35–42] for additional information on sample fabrication, characterization, and experimental methods.

[36] K.-Q. Lin, J. Holler, J. M. Bauer, P. Parzefall, M. Scheuck, B. Peng, T. Korn, S. Bange, J. M. Lupton, and C. Schüller, Large-scale mapping of moirésuperlattices by hyperspectral raman imaging, Adv. Mater. **33**, 2008333 (2021).

[37] M. Yamamoto, S. Dutta, S. Aikawa, S. Nakaharai, K. Wakabayashi, M. S. Fuhrer, K. Ueno, and K. Tsukagoshi, Self-limiting layer-by-layer oxidation of atomically thin WSe_2, Nano Lett. **15**, 2067 (2015).

[38] C. Tan, Y. Liu, H. Chou, J. S. Kim, D. Wu, D. Akinwande, and K. Lai, Laser-assisted oxidation of multi-layer tungsten diselenide nanosheets, Appl. Phys. Lett. **108**, 083112 (2016).

[39] H. Li, G. Lu, Y. Wang, Z. Yin, C. Cong, Q. He, L. Wang, F. Ding, T. Yu, and H. Zhang, Mechanical exfoliation and characterization of single- and few-layer nanosheets of WSe_2, TaS_2, and $TaSe_2$, Small **9**, 1974 (2013).

[40] P. Giannozzi *et al.*, QUANTUM ESPRESSO: A modular and open-source software project for quantum simulations of materials, J. Phys. Condens. Matter **21**, 395502 (2009).

[41] P. Giannozzi *et al.*, Advanced capabilities for materials modelling with Quantum ESPRESSO, J. Phys. Condens. Matter **29**, 465901 (2017).

[42] T. Sohier, M. Calandra, and F. Mauri, Density functional perturbation theory for gated two-dimensional heterostructures: Theoretical developments and application to flexural phonons in graphene, Phys. Rev. B **96**, 075448 (2017).

[43] K. Berland, V. R. Cooper, K. Lee, E. Schröder, T. Thonhauser, P. Hyldgaard, and B. I. Lundqvist, Van der Waals forces in density functional theory: A review of the vdW-DF method, Rep. Prog. Phys. **78**, 066501 (2015).

[44] T. A. de Jong, J. Jobst, H. Yoo, E. E. Krasovskii, P. Kim, and S. J. van der Molen, Measuring the local twist angle and layer arrangement in Van der Waals heterostructures, Phys. Status Solidi (b) **255**, 1800191 (2018).

[45] P. V. Nguyen, N. C. Teutsch, N. P. Wilson, J. Kahn, X. Xia, A. J. Graham, V. Kandyba, A. Giampietri, A. Barinov, G. C. Constantinescu, N. Yeung, N. D. M. Hine, X. Xu, D. H. Cobden, and N. R. Wilson, Visualizing electrostatic gating effects in two-dimensional heterostructures, Nature (London) **572**, 220 (2019).

[46] B. Amin, T. P. Kaloni, and U. Schwingenschlögl, Strain engineering of WS_2, WSe_2, and WTe_2, RSC Adv. **4**, 34561 (2014).

[47] T. Brumme, M. Calandra, and F. Mauri, First-principles theory of field-effect doping in transition-metal dichalcogenides: Structural properties, electronic structure, Hall coefficient, and electrical conductivity, Phys. Rev. B **91**, 155436 (2015).

[48] J. Voit, L. Perfetti, F. Zwick, H. Berger, G. Margaritondo, G. Grüner, H. Höchst, and M. Grioni, Electronic structure of solids with competing periodic potentials., Science **290**, 501 (2000).

[49] S. Moser, An experimentalist's guide to the matrix element in angle resolved photoemission, J. Electron Spectrosc. Relat. Phenom. **214**, 29 (2017).

[50] S. Lisi *et al.*, Observation of flat bands in twisted bilayer graphene, Nat. Phys. **17**, 189 (2021).

[51] https://doi.org/10.26037/yareta:3zalm3iglrbmtiubgxqhrhn2sq.